Journal of Physics D: Applied Physics

Check for updates

OPEN ACCESS

RECEIVED
6 November 2025

REVISED
28 January 2026

ACCEPTED FOR PUBLICATION
5 February 2026

PUBLISHED
16 February 2026

Original content from this work may be used under the terms of the Creative Commons Attribution 4.0 licence.

Any further distribution of this work must maintain attribution to the author(s) and the title of the work, journal citation and DOI.

PAPER

# Triple evaporation growth of sodium–potassium–antimonide thin films as photoemission source for electron accelerators

C Wang[1,2], J Dube[1,3,*], A Galdi[1,4], T Kamps[1,3] and J Kühn[1]

[1] Helmholtz-Zentrum Berlin für Materialien und Energie GmbH, Hahn-Meitner-Platz 1, 14109 Berlin, Germany
[2] Universität Siegen, Institut für Werkstofftechnik, Paul-Bonatz-Straße 9-11, 57076 Siegen, Germany
[3] Humboldt-Universität zu Berlin, Institut für Physik, Newton-Straße 15, 12489 Berlin, Germany
[4] Dipartimento di Ingegneria Industriale, Università degli Studi di Salerno, 84084 Fisciano (SA), Italy
[*] Author to whom any correspondence should be addressed.

**E-mail:** jonas.dube@helmholtz-berlin.de and julius.kuehn@helmholtz-berlin.de

**Keywords:** photocathodes, thin film, bi-alkali antimonide, thermal evaporation deposition, stoichiometry control, x-ray photoelectron spectroscopy

Supplementary material for this article is available online

## Abstract

Bi-alkali antimonide photocathodes are promising candidates for use as electron sources in high-brightness applications at advanced accelerator facilities. However, their preparation remains challenging due to the narrow compositional window required for optimal performance. We addressed these challenges by using a newly developed deposition system that employs effusion cells for precise flux control. In this work, we present a triple evaporation growth procedure for the preparation of $Na_2KSb$ photocathodes. This method significantly improves reproducibility compared to the traditional sequential growth process. The systematic growth of four photocathodes with varying stoichiometry demonstrated precise control over the chemical composition. Detailed x-ray photoelectron spectroscopy analysis, combined with measurements of spectral quantum efficiency and lifetime, revealed strong correlations between the stoichiometry and photoelectric properties. Quantum efficiencies exceeding 5% and $1/e$ lifetimes longer than 500 h were achieved. A $Na_2KSb$ photocathode produced using this method was used for the commissioning of the photoinjector at the SEALab accelerator, demonstrating the operation of an SRF photoinjector with a sodium-based photocathode for the very first time.

## 1. Introduction

State-of-the-art and future electron accelerators such as energy recovery linacs [1, 2], free electron lasers [3, 4], or ultra-fast electron diffraction [5] facilities have increasing demands on the electron source. To meet the specific requirements, photocathodes are used, which can be metals (Cu, Mg) or thin films of high efficiency photoemitters. The thin films are usually deposited on metal via thermal evaporation. Multi-alkali antimonide photocathodes are suitable candidates for high-brightness applications due to their high quantum efficiency (QE) in the visible regime and low intrinsic emittance [6]. Cs–K–Sb in particular has been reported capable for high-current operation with an operational lifetime over a month in SRF and DC-SRF guns [7, 8].

Further studies in the field are focused on an increased robustness and epitaxial growth of the photocathodes [9–13]. Na–K–Sb photocathodes have demonstrated quantum efficiencies comparable to those of Cs–K–Sb in the visible, with QE values reaching several percent in the green [14, 15]. Additionally, superior thermal robustness compared to Cs–K–Sb was observed in Na–K–Sb photocathodes, satisfying the suitability for high-current operations [16]. However, over the past decades, its widespread application in photoinjectors has been hindered by poor reproducibility and success rate, resulting in significant variations in QE between growths. These challenges stem from three key issues: (1) the narrow stoichiometric window required for high QE, (2) extremely low equilibrium vapor pressure of

© 2026 The Author(s). Published by IOP Publishing Ltd

Na for $Na_2KSb$ phase, and (3) the lack of precise parameter control, particularly alkali metal flux rate. At Helmholtz–Zentrum Berlin für Materialien und Energie GmbH (HZB) the photocathode laboratory has been upgraded in 2024 to overcome these challenges [17]. The traditional synthesis of Na–K–Sb is based on the sequential evaporation of the Sb, followed by K and Na, which react with the Sb layer forming the bialkali compound. The typical setup employs alkali metal dispensers, where the alkali flux is controlled by the applied current to the dispensers and the flux stability is poor. The improved preparation system employs effusive cells, which can precisely control the molecular flux by temperature, and allows the simultaneous deposition of all three materials, with added flexibility in choice of the procedure [16, 18].

In this paper, we present a triple evaporation method (i.e. the simultaneous deposition of all three elements) for $Na_2KSb$ photocathodes that demonstrates high reproducibility and allows the deposition of high QE, long lifetime photocathodes. We show multiple photocathodes grown using these procedures with quantum efficiencies ranging from 3% to more than 6% and discuss the correlation between stoichiometry, measured *in-situ* via x-ray photoelectron spectroscopy (XPS), QE and dark lifetime. Finally, we demonstrate the operation of an SRF photoinjector with a $Na_2KSb$ photocathode in section 5. The insights gained from this work contribute to the broader understanding of composition control, and performance optimization in alkali-antimonide thin films, relevant to other photoemissive and optoelectronic materials.

## 2. Experimental setup

Bi-alkali antimonide photocathodes have been researched at HZB for years [18–20]. An improved preparation system was set up in 2024 to overcome the limitations described in section 1 [17]. This system enables the simultaneous deposition of three materials. The antimony (Sb) is evaporated from a thermal cracker cell (TCC) located at 148 mm distance at an angle of 52° to the normal of the substrate surface. It is equipped with Alfa Aesar Sb beads with 99.999% purity. The sodium (Na) and potassium (K) are evaporated from effusion cells from MBE Komponenten mounted with an angle of 30° to the substrate normal as shown in figure 1. The distance can be varied by a $z$-drive and is usually set to 60 mm during the growth. Each effusion cell is loaded with five SAES AlkaMax Pills, which can be handled under air when refilling the sources, and release high purity alkali metals when heated. No additional contaminants were found in XPS spectra. The effusion cells provide a better control of the flow rates compared to dispensers used in the previous deposition system at HZB. The base pressure of the preparation system is below $1 \times 10^{-10}$ mbar. A water cooled quartz crystal microbalance (QCM) can be placed at the same position as the photocathode substrate to measure the deposition rate prior to each growth. This enhances the potential for the development of new growth procedures and improves the reproducibility. During the growth, an aperture with an 8 mm diameter hole and beveled edges is positioned in front of the 10 mm diameter plug to avoid any material being deposited onto the edge of the plug. This is crucial for the operation of the photocathode in a photoinjector to reduce multipacting and field emission.

When starting the growth, the photocathode is illuminated with a 520 nm laser to be more sensitive for the small photocurrent at the beginning of the deposition. Later on, the light source is changed to a spectral response setup, which consists of a Xenon lamp and a monochromator. This light source has a significantly lower power, but allows the investigation of the QE from 380 to 700 nm with 5 nm bandwidth.

Directly below the preparation chamber, an XPS analysis chamber is attached. The transfer process is conducted under UHV conditions with a pressure maintained in the $10^{-10}$ mbar range. During the XPS the pressure increases to low $10^{-9}$ mbar due to degassing of the filaments, resulting in a typical QE decay by about 50% after the XPS measurements. All XPS measurements presented in this article has been performed with Al K$\alpha$ with an applied power at the anode of 250 W. The stoichiometry and binding energy information has been determined from high resolution region scans of the Na 1s (1065–1087) eV, K 2p (288–310) eV and Sb 3d (522–550) eV spectra. The intensity associated to each region was obtained via numerical integration of the curves after subtracting a Shirley background. Details on the procedure and integration interval are reported in the supplementary material. Since the Na $KL_1L_{23}$ Auger peak falls into the Sb 3d integration region, the error introduced by including the associated spectral weight has been estimated by decomposing the spectra in pseudo-Voigt components and resulted to be about 12% (details are given in the supplementary material). It should be noted, that the inelastic mean free path (IMFP) of photoelectrons from Na 1s is just 15.9 Å while the IMFP for K 2p and Sb 3d are 35.4 Å and 29.9 Å, respectively [21, 22]. Therefore, the characterization depth of Na is smaller compared to K and Sb. For the calculation of the stoichiometry we consider the Na–K–Sb film as a homogeneous layer and

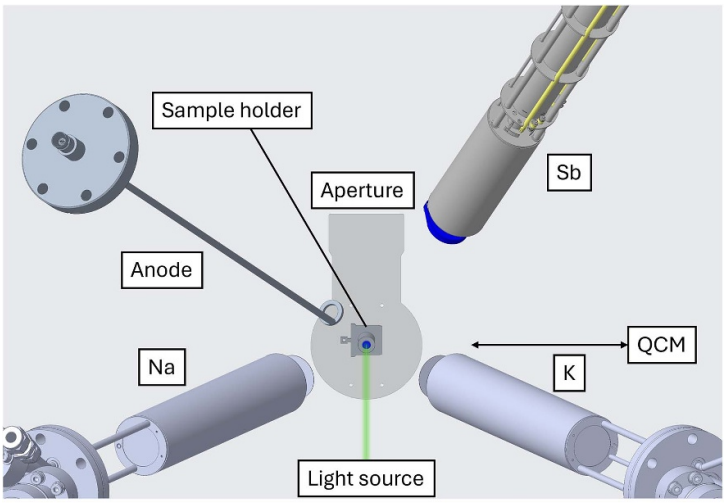


**Figure 1.** Schema of the deposition geometry of our triple evaporation setup. The water-cooled quartz crystal microbalance (QCM) can be moved into the sample position, to calibrate the deposition rates.

the chemical composition ratio of $A$ (K or Na) and $B$ (Sb) is calculated by equation (1),

$$\frac{c[A]}{c[B]} = \frac{I[A]}{I[B]} \cdot \frac{\sigma[B] \cdot \lambda[B] \cdot T[B]}{\sigma[A] \cdot \lambda[A] \cdot T[A]}, \tag{1}$$

where $c$ is the chemical concentration of the selected element and $I$ is the signal intensity (peak area after background subtraction) of a specific electron orbital. The parameter $\sigma$ is the photoionization cross section [23], $\lambda$ the IMFP of the specific material and $T$ the transmission function of the electron analyzer (SPECS Phoibos 100 CCD).

## 3. Triple evaporation growth

The substrate material and geometry of the plug is chosen with respect to the operational conditions in the SRF photoinjector. While the plugs for the photoinjector can only used once, we have additional test plugs with similar properties, which can be cleaned and reused. The same molybdenum (Mo) plug was used as the substrate for all TWH-series photocathodes presented in this paper. The Mo substrate is mechanically polished using diamond and silica suspensions to achieve a surface roughness of approximately $R_q \approx 10\,\text{nm}$. Before each growth, the Mo substrate is heated to 550 °C and afterwards sputtered with argon ions to ensure a clean surface. This process is repeated until no contamination peaks, such as oxygen or carbon are detected in the XPS spectrum of the uncoated plug. Before the growth, the deposition rate is measured with the QCM and the growth temperatures for the three sources are selected to achieve a flow rate of $0.01\,\text{Å}\,\text{s}^{-1}$ for Sb, $0.04\,\text{Å}\,\text{s}^{-1}$ for Na and $0.14\,\text{Å}\,\text{s}^{-1}$ for K. The cracker of the Sb TCC is heated to 700 °C and the tube is at 650 °C. The alkali metal flux gradually decreases with repeated use of the source pills. Consequently, the effusion cell temperatures must be adjusted prior to each new growth, to achieve the same deposition rate. However, within a single growth the flux remains sufficiently stable, such that the temperatures can be held constant. This progressive reduction of the deposition rate probably accounts for the observed variation in the time needed to achieve the maximum QE across the different cathodes. After approximately ten growth cycles with the same set of AlkaMax pills, the sources become partially depleted, and additional manual temperature adjustments may be required even during a single growth.

So far, experiments demonstrated, that the best performance can be achieved by growing the photocathodes in three steps: (I) triple evaporation, (II) compensation of Na excess on the surface and (III) cool down in K flux. By evaporating only K and Sb during phase II, a Na rich surface can be avoided, which significantly increases the photocathode lifetime. Additionally, evaporating K in the first stages of the cool down phase is required as a sudden closure of the K shutter would cause a re-evaporation of the potassium at the high substrate temperatures required for the formation of the correct Na–K–Sb compound in phase I and II. Therefore the evaporation will be continued, until the sample is sufficiently cooled down. The growth procedure for the presented four $Na_2KSb$ photocathodes is summarized in figure 2 with a detailed description of the three phases below.

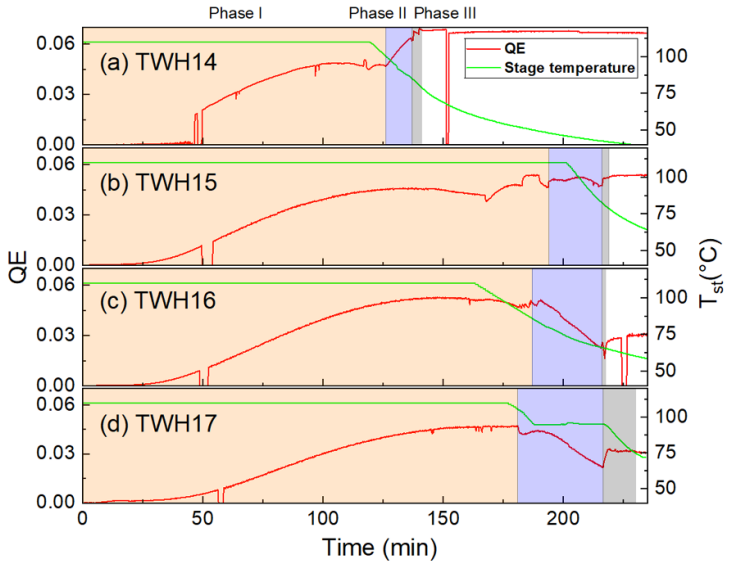


**Figure 2.** QE (at 520 nm) and stage temperature in triple evaporation growth of the presented photocathodes. The growth process is structured in three phases. For this study, the chemical composition was varied by the duration of phase II. (a) TWH14, (b) TWH15, (c) TWH16 and (d) TWH17.

Phase I is the simultaneous evaporation (triple evaporation) of all three materials while the temperature of the sample stage is set to 110 °C. It should be noted, that the surface temperature of the substrate differs from the stage temperature, as it is additionally heated by the evaporators, in particular the cracker of the Sb TCC. The QE is tracked during the growth and shown in figure 2. An increase of the photocurrent can usually be observed around 10 min after the shutters of the three sources have been opened. The thickness of the photocathode is mainly determined by the evaporation time in phase I and can be calculated from the Sb deposition rate of 0.01 Å, assuming a sticking coefficient of 1 as described by Liang [24]. The thickness of the final $Na_2KSb$ can be estimated from this value with the 3.8 times space expansion rate from metallic Sb to cubic $Na_2KSb$ crystal structure [25]. Usually, the maximum QE is reached after 100–150 min and the QE might decrease after reaching its peak. At the end of this phase, the Na and K shutters are closed and opened to maximize the QE which usually reaches a value around 4.5%.

During phase II the Na shutter is closed and only K and Sb are evaporated onto the substrate. This step is required to obtain the ideal stoichiometry and improved QE and lifetime of the photocathode. The deposition time in phase II has been varied from 10 to 35 min to study the correlation between the different growth parameters with the stoichiometry and the photoelectric properties including QE and dark lifetime.

The goal of phase III is to cool down the photocathode and stop the deposition without significant reduction of the QE. The Sb shutter is closed and the heater of the sample stage is turned off to cool down the photocathode to room temperature. Alkali deficiency has a negative effect to the QE and dark lifetime of the photocathode [17]. Therefore, the K shutter is kept open at a reduced deposition rate, approximately 10 °C lower then in phase I. K is evaporated until the QE plateaus or the stage temperature is below 70 °C.

## 4. Results and discussion

The growth procedure described above has been used to grow four photocathodes with different stoichiometries by systematically varying the duration of phase II. The Sb evaporation in phase II was increased for each photocathode from 0.7 nm for TWH14, to 1.3 nm, 1.8 nm and 2.2 nm for the photocathodes TWH15, TWH16 and TWH17, respectively. The duration of phase II is expressed in terms of the equivalent Sb thickness, since the Sb deposition rate can be measured more accurately with the QCM, whereas the alkali deposition rates are harder to quantify due to an unknown sticking coefficient. All photocathodes were monitored for 4 d after the growth, to determine the $1/e$ dark lifetime. The monitoring time is required to obtain a reliable calculation of the photocathode lifetime. Afterwards,

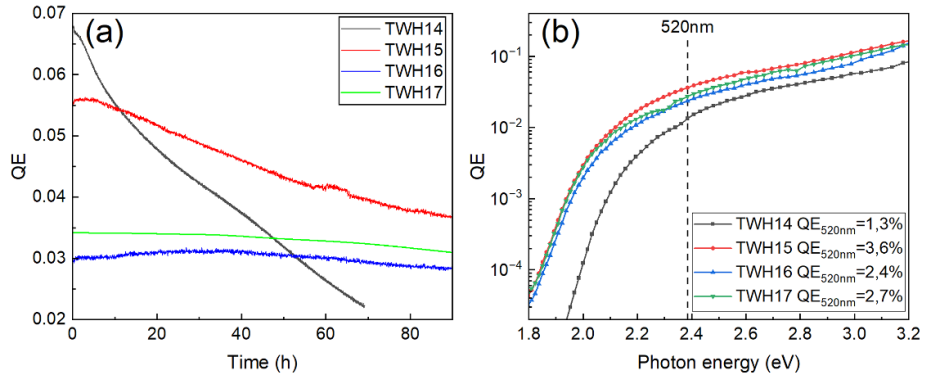


**Figure 3.** Dark lifetime (a) and spectral response (b) of four $Na_2KSb$ photocathodes. The spectral response data were taken 4 d after growth. Significant differences can observed, due to the different chemical composition of the photocathodes.

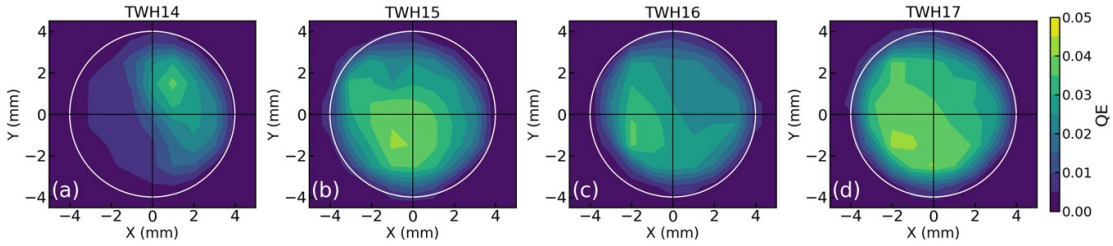


**Figure 4.** QE maps of $Na_2KSb$ photocathodes measured at 520 nm 4 d after growth: (a) TWH14, (b) TWH15, (c) TWH16, (d) TWH17. The gradient of the QE maps correlates with the chemical composition.

spectral response and XPS measurements were done. In this section, we describe the results of this systematic study and will discuss correlations between the photoelectric properties and the stoichiometry of the photocathodes.

### 4.1. Photoelectric properties

The peak QE and the dark lifetime are measured in the center of the photocathode, at the same position where the photocurrent has been measured during the growth. The peak QE is the highest QE the photocathode achieved after the growth has been finished (all shutters closed). The dark lifetime $\tau$ is measured as soon as the sample stage temperature is below 50 °C by fitting $\mathrm{QE} = A \times \exp(-t/\tau)$, with $t$ the time, and $A$ representing the initial QE. The lifetime measurements are shown in figure 3(a) and summarized in table 1. While the photocathode TWH14 achieved $\mathrm{QE}_{\mathrm{peak}} = 6.8\%$, the $1/e$ lifetime was just 63 h. TWH15 achieved a lifetime of $\tau = 190$ h with $\mathrm{QE}_{\mathrm{peak}} = 5.6\%$ and the photocathodes TWH16 and TWH17 reached a lifetime of more then 500 h with a QE larger 3%. Please note that extrapolating such lifetimes from just 4 d of measurement is becoming increasingly difficult. Therefore, we only state that the lifetime of these photocathodes is greater than 500 h. The spectral response curves in figure 3(b) show a very similar course. The QE values in this plot differ from the peak QE, as the spectral response has been measured 4 d after the growth. The curve for TWH14 is significantly suppressed across the measured spectrum, consistent with its shorter dark lifetime. In contrast, the spectra for TWH15, TWH16, and TWH17, while similar, exhibit distinct fine structures: the QE of TWH15 rises more rapidly between 2.1 and 2.5 eV.

The homogeneity of the QE distribution is determined by QE maps 4 d after the growth as shown in figure 4. The maps has been measured at 520 nm with a light spot size of 2 mm diameter and a step size of 1 mm. It must be noted that the highest QE is not necessarily in the center of the photocathode. Due to the angles of the evaporators to the surface normal, a gradient of the chemical composition can occur on the photocathode due to different deposition rates along the surface. As we know, that a high QE is restricted to a narrow stoichiometric window, this also results in variations of the QE over the whole photocathode area [14, 26]. As the Na evaporator is positioned on the left side, and K on the right, the Na/K ratio decreases from left to right across the photocathode surface. The Sb source is mounted in the top right, resulting in a diagonal Na/Sb gradient from the bottom-left to the top-right. As shown in figure 4, this diagonal gradient is also reflected in the QE maps, indicating that the QE is more strongly

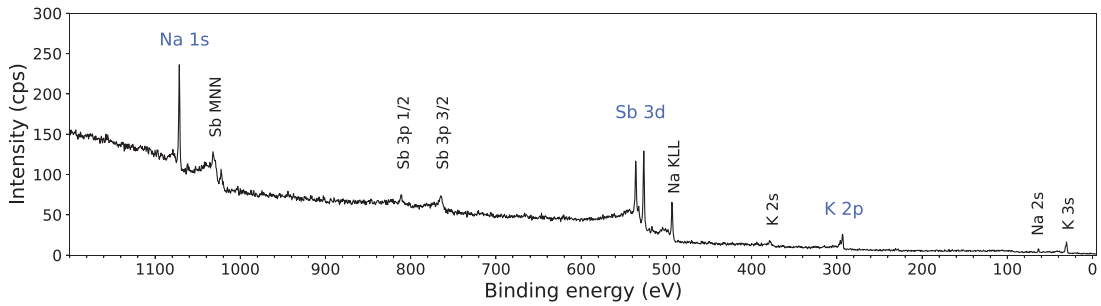


**Figure 5.** XPS survey spectrum of the photocathode TWH14 measured with Al K$\alpha$. The peaks used for the quantification of the stoichiometry are marked in blue.

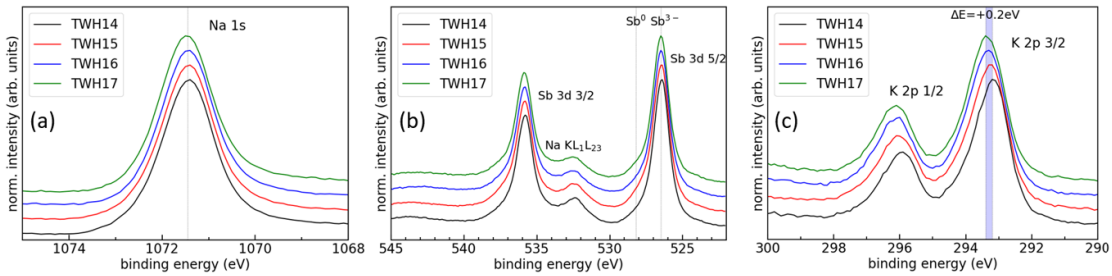


**Figure 6.** Al K$\alpha$ XPS spectra of four $Na_2KSb$ photocathodes synthesis by triple evaporation method. (a), (b) and (c) are the region scans of Na 1s, K 2p and Sb 3d, respectively. All spectra taken after the spectral response data at day 4.

correlated with the Na/Sb ratio than with the Na/K ratio. To further investigate the compositional origin of this trends, XPS measurements were performed.

### 4.2. XPS analysis

The XPS measurements have been performed after the photoelectric measurements, as the QE drops during the XPS. This is caused by an increased pressure, since the bypass of the x-ray gun is located directly in front of the sample position. In figure 5(a) survey of the photocathode TWH14 is shown. The spectrum shows a high purity of the film without any detectable contaminants. High resolution region scans were used for the further analysis and quantification of the stoichiometry. The corresponding peaks are annotated in blue in the survey. As shown in figure 6, the peak positions and peak widths of the three elements maintain a high consistency, indicating a very good reproducibility of the triple evaporation growth procedure. In figure 6(a) the Na-spectra of all four photocathodes are shown, with a consistent binding energy of the Na 1s peak of 1071.5 eV. Figure 6(b) shows the region scans of Sb 3d with annotations of $Sb^0$, $Sb^{3-}$ peaks locating in 528.2 eV and 526.5 eV. The peak position of $Sb^0$ was previously measured by deposition of Sb on the same Mo plug, with its peak position corresponding to metallic Sb [19, 27, 28]. For the four $Na_2KSb$ photocathode, the Sb $3d_{5/2}$ and Sb $3d_{3/2}$ main peak lies in 526.5 eV and 535.9 eV, respectively. A small second peak is located at a higher binding energy about 528.0 eV, corresponding to metallic Sb. This is likely due to a shadowing effect at the edge of the active area, caused by the aperture and the different angles of the evaporators. Anyhow, the area of the main peak reaches approximately 95% of the whole peak area.

The peak at 532.6 eV between the Sb 3d doublet peaks corresponds to the Na $KL_1L_{23}$ auger peak, which overlaps with the O 1s peak. The samples undergo negligible oxidation since no second peaks of Na or K oxides were found in their spectra, though the peak intensity of the O 1s peak is not measured directly.

The position of the K $2p_{3/2}$ in figure 6(c) increases from 293.2 eV for TWH14, 293.3 eV for TWH15 to 293.4 eV for the photocathodes TWH16 and TWH17, which is the only obvious difference between the four photocathodes in their XPS spectra. If the shifts in binding energy were attributed to changes in the band bending at the sample surface, we would expect to observe similar shifts for all the elements, and especially for Sb 3d, which has a probing depth close to the one of K 2p. Therefore, the shift in the K $2p_{3/2}$ peak is probably attributed to a different chemical environment. Indeed, a longer deposition of K-Sb in phase II from TWH14 to TWH17 causes a K-richer stoichiometry and possibly a larger extent

**Table 1.** Summary of growth parameters, stoichiometry and photoelectric properties of the four presented photocathodes. Thickness values are estimated from QCM measurements of Sb.

| Sample | Sb evaporation phase I | Sb evaporation phase II | Stoichiometry | Peak QE (center) | 1/e dark lifetime |
|---|---|---|---|---|---|
| TWH14 | 7.6 nm | 0.7 nm | $Na_{2.4}K_{1.0}Sb_{1.0}$ | 6.8% | 63 h |
| TWH15 | 11.6 nm | 1.3 nm | $Na_{2.2}K_{1.2}Sb_{1.0}$ | 5.6% | 220 h |
| TWH16 | 11.1 nm | 1.8 nm | $Na_{1.9}K_{1.2}Sb_{1.0}$ | 3.1% | >500 h |
| TWH17 | 10.9 nm | 2.2 nm | $Na_{1.9}K_{1.2}Sb_{1.0}$ | 3.4% | >500 h |

of phase transformation from $Na_2KSb$ to hexagonal $NaK_2Sb$. The detailed investigation of this effect in a wider stoichiometry range is part of future research. The shown spectra has been used to calculate the stoichiometry of the photocathodes as described in section 2 which is summarized in table 1.

### 4.3. Correlation between stoichiometry and photoelectric properties

The causal relationship between the photoelectric properties and the stoichiometry is crucial for the development of new and improved photocathode materials. Finally the relation with the growth parameters is essential for a controlled and reproducible photocathode growth. The parameters of the four photocathodes are summarized in table 1. The Sb thickness was estimated by QCM measurements prior each growth. The photocathode TWH14 achieved the highest QE of 6.8% but the shortest lifetime of only 63 h. This behavior correlates with its high Na surface concentration with $Na/Sb = 2.4$ and $(Na + K)/Sb = 3.4$, deviating from the ideal stoichiometry of $Na_{2.0}K_{1.0}Sb_{1.0}$. The highest QE of TWH14 is observed in the top-right region of figure 4(a), opposite to the position of the Na effusion cell (see figure 1). This spatial distribution supports the conclusion of Na excess of this sample, as the lowest Na/Sb ratio occurs in this area. The low QE in the bottom-left region after 4 d further suggests that Na enrichment accelerates the QE degradation.

For the following photocathodes the Na content was reduced step by step, by increasing the duration of phase II. This was verified by the stoichiometry from XPS measurements as shown in table 1 demonstrating the reproducible and sensitive control of the photocathode growth. The photocathodes TWH15–TWH17 achieved a significantly improved lifetime of 220 h for TWH15, and more then 500 h for TWH16 and TWH17, but at the cost of a reduced QE. For TWH15 the Na/K ratio is closest to the envisaged value of 2, showing the most homogeneous QE map. For the photocathodes TWH16 and TWH17 the gradient in the QE map has changed, due to an excess of K and an Na deficiency. Therefore, the highest QE occurred at the same side as the Na effusion cell.

These results reveal the limitation of this procedure. While a high QE requires a stoichiometry close to $Na_2KSb$, for long lifetime the enrichment of Na on the surface should be avoided. The reduced temperature during phase II in the initial procedures probably induced an unwanted formation of $NaK_2Sb$ layer on the surface. This resulted in a significant reduction of the QE, due to the low intrinsic QE of the $NaK_2Sb$ phase. To overcome this limitation, we optimized the growth procedure with a higher substrate temperature in phase II. This modification is designed to relieve the Na surface enrichment and suppress the formation of $NaK_2Sb$ phase, achieving better compatibility between QE and dark lifetime, as demonstrated for the photocathode SEA03 in section 5.

## 5. First operation in an SRF photoinjector

The triple evaporation method has been used to prepare a photocathode for the commissioning of the SRF photoinjector at the Sustainable Electron Accelerator Laboratory (SEALab, formerly bERLinPro) [2, 29, 30] due to its good reproducibility, high QE and long lifetime. For this photocathode a Molybdenum plug with a different geometry is used, which is specifically adapted for the use in the SRF photoinjector [31]. While the outer form factor is similar, this plug contains an additional mechanical interface for the SRF gun. A reduced sample stage temperature of 100 °C was used during the growth, due to the different geometry and thus thermal conductivity of the plug. Experiments verified, that this temperature corresponds to the same temperature at the substrate surface as the photocathodes described earlier. At the system, the Na and K effusion cells have been swapped so that the angle between the Na and Sb evaporators are reduced, resulting in a reduced Na/Sb gradient. The growth procedure has been adjusted to achieve a better compatibility between performance and stability and is shown in figure 7. In phase I all three materials have been evaporated for about 200 min, resulting in an Sb thickness of 12 nm. In phase II, additional Sb and K was evaporated for 7 min (0.4 nm Sb), while the Na shutter has been closed. With the adjusted procedure, the stage temperature was not reduced but the same as during phase I, to

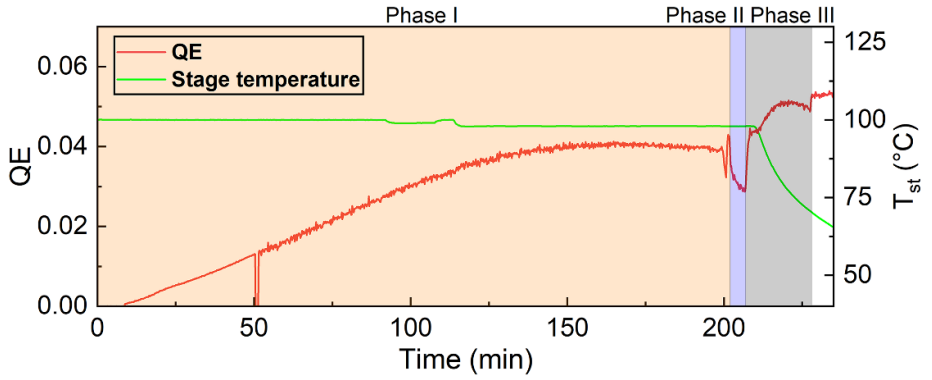


**Figure 7.** The growth procedure of photocathode SEA03 prepared for the commissioning of SEALab, resulting in a QE of 5.4% at 520 nm.

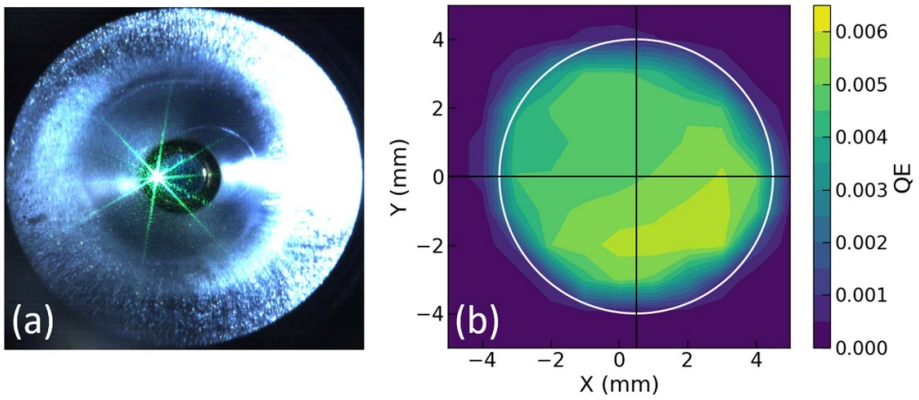


**Figure 8.** (a) The photocathode is shown in the center of the back wall of the superconducting niobium cavity (1.8 K) with the 521 nm photocathode laser reflecting at the edge of the cathode plug (80 K). (b) The QE map of the SEA03 photocathode measured 4 d after insertion into the SRF-photoinjector via the drain current at 5 kV DC bias. It has a QE = 0.42% in the center.

enhance the formation of more homogeneous $Na_2KSb$ layers during this phase. In phase III the Sb shutter was closed and the sample cooled down, while K was evaporated for few more minutes at a lower deposition rate. One day after growth the QE was measured to be 5.4% in the center of the film.

As the photocathode had to be used in the photoinjector, it was only monitored for one night, and no XPS measurements were performed in order to avoid damaging the photocathode. The photocathode was very stable over night with a $1/e$ lifetime of more then 500 h. To move the photocathodes from the laboratory to the the SEALab accelerator, a compact UHV vacuum suitcase with a base pressure of $2 \times 10^{-11}$ mbar has been used. A transfer system is attached to the photoinjector and to the preparation chamber to load and unload the suitcase [32]. Unfortunately, a pincer malfunctioned which delayed the photocathode transfer. The photocathode was inserted into the cold part of the photoinjector 14 d after growth. During this process, the photocathode is cooling down from room temperature to the operation temperature of 80 K. In the photoinjector, the QE is measured by the drain current with a constant applied voltage of 5000 V. The RF-field is turned off during the QE measurements. The photocathode laser with 521 nm wavelength was operated at 1 MHz repetition rate, a bunch length of 4 ps and a power of about 1 mW. The laser can be scanned over the photocathode surface by motorized mirrors for a spatially resolved measurement.

In figure 8(a) the photocathode is shown in the cavity with the laser reflecting at the edge of the cathode plug. The QE map in figure 8(b) has a maximum QE of 0.58% located in the lower right region and a QE = 0.42% in the center. This value is about one order of magnitude smaller then the QE measured in the photocathode laboratory after growth. The degradation is mainly attributed to the long transfer time of two weeks after preparation and an increased residual gas exposure during the extended transfer. The photocathode was operated for the commissioning of the SEALab accelerator showing promising results. A detailed analysis of the operational performance is currently under investigation.

## 6. Conclusion

In the past, the growth of Na–K–Sb photocathodes was hindered by a poor reproducibility and therefore a strong variation in QE and lifetime between the growths. A preparation system and a triple evaporation growth procedure has been developed to overcome these challenges. This approach has yielded a significant improvement in reproducibility over traditional sequential methods. Furthermore, we proved the feasibility of precise stoichiometric control within the narrow optimal stoichiometric window, enabling the enhancement of QE and dark lifetime. Our results reveal the correlations between specific growth parameters, the final stoichiometry, and the resulting photoelectric properties.

A set of four photocathodes with varying stoichiometry has been grown by controlled variation of the growth parameters. A Na excessive sample showed a QE of 6.8% but a very short lifetime of just 63 h. Samples with increased duration of phase II achieved a significantly longer lifetime up to more then 500 h, but at the cost of a reduced QE down to 3%. These results emphasize the narrow stoichiometric window which has to be achieved in order to obtain a high QE, long lifetime photocathode.

With just minor optimizations of the growth procedure, we fabricated a photocathode (SEA03) that achieved a peak QE of 5.4% at 520 nm and a dark lifetime exceeding 500 h at the center of the film. This photocathode was used as electron source for SEALab, demonstrating the use of Na–K–Sb photocathodes in an SRF photoinjector for the very first time. Current research is focused on further refining the growth procedure of Na–K–Sb photocathodes and comprehensively evaluating their operational performance in the SRF photoinjector at SEALab. Altogether, these results provide valuable insights for the controlled preparation of photocathodes for high-current, low-emittance applications. They pave the way for next-generation high-performance photocathodes for state-of-the-art and future accelerator facilities and contribute to the development of improved photoemissive materials.

## Data availability statement

The data cannot be made publicly available upon publication because they are not available in a format that is sufficiently accessible or reusable by other researchers. The data that support the findings of this study are available upon reasonable request from the authors.

XPS Peak Area Calculation available at https://doi.org/10.1088/1361-6463/ae4246/data1.

## Acknowledgments

We thank Axel Neumann, Michael Schuster and André Frahm from HZB for their support during the photocathode transfer. We thank Guido Klemz from HZB for his support during the QE measurements in the SRF-photoinjector.

## Funding

This work was funded by the Deutsche Forschungsgemeinschaft (DFG)—Project Number 490940284, the German Bundesministerium für Forschung, Technologie und Raumfahrt, Land Berlin and grants of the Helmholtz Association.

## Conflict of interest

The authors declare no conflicts of interest.

## Author contributions

C Wang 0009-0000-4125-0303
Conceptualization (lead), Data curation (lead), Formal analysis (lead), Investigation (equal), Writing – original draft (equal), Writing – review & editing (equal)

J Dube 0000-0003-1052-9824
Conceptualization (equal), Data curation (equal), Formal analysis (equal), Investigation (equal), Writing – original draft (equal), Writing – review & editing (equal)

A Galdi 0000-0003-2863-5393
Conceptualization (supporting), Investigation (supporting), Writing – review & editing (equal)

T Kamps 0000-0002-5122-2290
Funding acquisition (lead), Project administration (equal), Supervision (equal), Writing – review & editing (equal)

J Kühn 0000-0003-3744-9242
Conceptualization (equal), Investigation (equal), Project administration (equal), Supervision (lead)

## References

[1] Zhao Z T, Wang Z, Feng C, Chen S and Cao L 2021 Energy recovery linac based fully coherent light source *Sci. Rep.* **11** 23875
[2] Neumann A *et al* 2022 bERLinPro becomes SEALab: status and perspective of the energy recovery linac at HZB *Proc. IPAC'22* pp 1110–3
[3] Emma P *et al* 2010 First lasing and operation of an Ångstrom-wavelength free-electron laser *Nat. Photon.* **4** 641–7
[4] Schaber J, Xiang R and Gaponik N 2023 Review of photocathodes for electron beam sources in particle accelerators *J. Mater. Chem.* **11** 3162–79
[5] Filippetto D, Musumeci P, Li R K, Siwick B J, Otto M R, Centurion M and Nunes J P F 2022 Ultrafast electron diffraction: visualizing dynamic states of matter *Rev. Mod. Phys.* **94** 045004
[6] Dowell D H, Bazarov I, Dunham B, Harkay K, Hernandez-Garcia C, Legg R, Padmore H, Rao T, Smedley J and Wan W 2010 Cathode R&D for future light sources *Nucl. Instrum. Methods Phys. Res. A* **622** 685–97
[7] Jia H *et al* 2024 High-brightness megahertz-rate beam from a direct-current and superconducting radio-frequency combined photocathode gun *Phys. Rev. Res.* **6** 043165
[8] Petrushina I *et al* 2020 High-brightness continuous-wave electron beams from superconducting radio-frequency photoemission gun *Phys. Rev. Lett.* **124** 244801
[9] Guo L *et al* 2025 Improved robustness of sequentially deposited potassium cesium antimonide photocathodes achieved by increasing the potassium content towards theoretical stoichiometry *Sci. Rep.* **15** 2900
[10] Parzyck C *et al* 2022 Single-crystal alkali antimonide photocathodes: high efficiency in the ultrathin limit *Phys. Rev. Lett.* **128** 114801
[11] Parzyck C T *et al* 2023 Atomically smooth films of CsSb: a chemically robust visible light photocathode *APL Mater.* **11** 101125
[12] Stam W G *et al* 2024 Growth of ultra-flat ultra-thin alkali antimonide photocathode films *APL Mater.* **12** 061114
[13] Pennington C A *et al* 2025 A structural analysis of ordered $Cs_3Sb$ films grown on single crystal graphene and silicon carbide substrates *APL Mater.* **13** 011120
[14] Sommer A 1955 New photoemissive cathodes of high sensitivity *Rev. Sci. Instrum.* **26** 25–726
[15] Spicer W E 1958 Photoemissive, photoconductive and optical absorption studies of alkali-antimony compounds *Phys. Rev.* **112** 114–114
[16] Cultrera L, Karkare S, Lillard B, Bartnik A, Bazarov I, Dunham B, Schaff W and Smolenski K 2013 Growth and characterization of rugged sodium potassium antimonide photocathodes for high brilliance photoinjector *Appl. Phys. Lett.* **103** 103504
[17] Dube J, Kühn J, Wang C, Mistry S, Klemz G, Galdi A and Kamps T 2025 Triple evaporation growth and photoemission characterization of bialkali antimonide photocathodes *J. Appl. Phys.* **138** 045704
[18] Mistry S, Kamps T, Kühn J and Wang C 2022 Multi-alkali antimonide photocathode development for high brightness beams *Proc. IPAC'22* pp 2610–3
[19] Schmeißer M A H, Mistry S, Kirschner H, Schubert S, Jankowiak A, Kamps T and Kühn J 2018 Towards the operation of Cs-K-Sb photocathodes in superconducting RF photoinjectors *Phys. Rev. Accel. Beams* **21** 113401
[20] Cocchi C, Mistry S, Schmeißer M, Amador R, Kühn J and Kamps T 2019 Electronic structure and core electron fingerprints of caesium-based multi-alkali antimonides for ultra-bright electron sources *Sci. Rep.* **9** 18276
[21] Werner W S M, Smekal W, Simperl F, Hronek M and Powell C J 2024 NIST Database for the Simulation of Electron Spectra for Surface Analysis (SESSA) *Version 2.2.2, NIST Standard Reference Database Number 100* (available at: https://nist.gov/srd/nist-standard-reference-database-100)
[22] Tanuma S, Powell C J and Penn D R 1994 Calculations of electron inelastic mean free paths. V. Data for 14 organic compounds over the 50–2000 eV range *Surf. Interface Anal.* **21** 165–76
[23] Scofield J H 1973 Theoretical photoionization cross sections from 1 to 1500 keV *Technical Report* (California Univ., Livermore. Lawrence Livermore Lab.)
[24] Liang X *et al* 2012 Deposition and in-situ characterization of alkali antimonide photocathodes *Proc. IPAC'12* (JACoW Publishing) pp 670–2
[25] Jain A *et al* 2013 Commentary: the materials project: a materials genome approach to accelerating materials innovation *APL Mater.* **1** 011002
[26] Spicer W E 1960 Photoemission and related properties of the alkali-antimonides *J. Appl. Phys.* **31** 2077–84
[27] Schubert S *et al* 2013 Bi-alkali antimonide photocathodes for high brightness accelerators *APL Mater.* **1** 032119
[28] Chastain J and King Jr R C 1992 Handbook of x-ray photoelectron spectroscopy *Perkin-Elmer Corporation* vol 40 p 25
[29] Kamps T *et al* 2023 Accelerator physics experiments at the versatile SRF photoinjector of SEALab *Proc. IPAC'23* pp 2115–8
[30] Kamps T *et al* 2025 First beam commissioning of the HZB SRF photoelectron gun *Proc. IPAC'25*
[31] Kühn J *et al* 2019 Thermal load studies on the photocathode insert with exchangeable plug for the bERLinPro SRF-photoinjector *Proc. SRF'19* (https://doi.org/10.18429/JACoW-SRF2019-TUP100)
[32] Kühn J *et al* 2017 UHV photocathode plug transfer chain for the bERLinPro SRF-photoinjector *Proc. IPAC'2017* (https://doi.org/10.18429/JACoW-IPAC2017-TUPAB029)